JOURNAL OF GEOPHYSICAL RESEARCH, VOL. 88, NO. C3, PAGES 1892-1908, FEBRUARY 28, 1983

A MODEL FUNCTION FOR OCEAN MICROWAVE BRIGHTNESS TEMPERATURES

F. J. Wentz

Remote Sensing Systems, Sausalito, California 94965

Abstract. We derive a relatively simple, yet accurate, relationship between the microwave brightness temperature of the ocean and conventional oceanographic and meteorological parameters. To begin with, the brightness temperature of the ocean and the intervening atmosphere is expressed in terms of integrals for the radiative scattering and emission from the sea surface and the radiative absorption and emission by the atmosphere. We then find closed-form approximations for these integrals and obtain a simplified model for the radiative transfer and scattering. The model is reduced to a function giving brightness temperature in terms of five variables: sea-surface temperature, sea-surface friction velocity, atmospheric columnar water vapor content, atmospheric columnar liquid water content, and surface air temperature. In the derivation of the model, the absorption coefficient for rain clouds and the wind-induced sea-surface emissivity are found from SEASAT SMMR observations. The remainder of the derivation is based on well-accepted microwave theory. The model function is referenced to the five frequencies and 49° incidence angle at which the SEASAT and Nimbus 7 SMMR operate. When compared with the more precise integral formulation, the model function accuracy is 0.2 K at 6.6 GHz and gradually degrades to 2.1 K at 37 GHz, horizontal polarization. These accuracies are an average over an ensemble of winds and atmospheres ranging from a specular surface and clear skies to a 21 m/s wind and a very heavy cloud layer containing 60 mg/cm² of liquid water, but excluding rain. An uncertainty of about 10% in the wind-induced emissivity introduces some additional error into the model function. Several of the derived model parameters are compared with values obtained in other experiments and theoretical investigations. The frequency ratios of the SMMR-inferred absorption coefficients for rain clouds are in very close agreement with that given by Mie scattering theory. The large-scale sea-surface slope variance found from the SMMR data is consistent with the slope variance computed from a sea wave spectrum, with that inferred from microwave scatterometer measurements at nadir, and with the Cox and Munk value deduced from sun glitter. The SMMR-inferred foam coverage correlates better with whitecap coverage than streak coverage, indicating that the increase in brightness temperature due to sea foam is more a result of whitecapping than streaking. A layered dielectric model for sea foam predicts the same frequency and polarization variation in the foam reflectivity as observed by the SMMR. The consistency of these results support the premise that the sea-surface emissivity is accurately represented by a composite model in which the emission from the rough, foam-free water is given by two-scale scattering theory and the foam emission is given by a layered dielectric theory.

Paper number 2C0410.
0148-0227/83/002C-0410$05.00

1. Introduction

At microwave frequencies, aircraft and satellite radiometers can measure the ocean brightness temperature (T_B) to within several tenths of degrees Kelvin in relative accuracy. Dual polarization, multi-frequency T_B observations at this accuracy contain significant information on the characteristics of the ocean surface and intervening atmosphere. The utilization of this information requires a knowledge of the relationship between T_B and conventional oceanographic and meteorological parameters. This T_B relationship has been expressed in many forms, ranging from complex scattering integrals [Wentz, 1975, Tsang et al., 1977] to simple linear expressions [Grody, 1976, Wilheit, 1980]. Our objective in this paper is to derive a relationship that retains the accuracy of the integral formulation while being simple enough to provide for rapid numerical computation. In this pursuit, we develop a model for approximating the radiative transfer and scattering. The model is reduced to a simple function containing no integrals. The utility of this model function is twofold. Firstly, for retrieving environmental parameters from an array of T_B's, it provides the 'A-matrix' of partial derivatives required by least squares estimation techniques [Bierman et al., 1978]. Secondly, because the model function is in terms of simple physical parameters, it provides insight into the relevant physics.

The T_B model function is referenced to the five frequencies (6.63, 10.69, 18, 21, 37 GHz) and the nearly constant incidence angle for the SEASAT (49° ± 0.5°) and Nimbus 7 (50° ± 0.5°) scanning multichannel microwave radiometers (SMMR). Horizontal and vertical polarization states (h-pol and v-pol) are considered, giving a total of 10 frequency/polarization channels. The T_B function can be interpolated to other frequencies and incidence angles, although such interpo-

lations are not discussed herein. The SEASAT SMMR data are used to derive two model components: the absorption coefficient for rain clouds and the wind-induced sea-surface emissivity. The remainder of the derivation is based on well-accepted microwave theory. There are five variables (arguments) in the function: sea-surface temperature T_s (K), sea-surface friction velocity U_* (cm/s), columnar water vapor content V (g/cm²), columnar liquid water content L (g/cm²), and surface air temperature T_a (K). The air temperature is of second-order importance relative to the other four variables. Note that the relationship between friction velocity and wind speed is approximately linear, and U_*= 100 cm/s corresponds to a 21 m/s wind measured at an altitude of 19.5 m in a neutrally stable atmosphere. The T_B model function is denoted by

$$T_B = f(T_s, U_*, V, L, T_a) \quad (1)$$

Equations (27) through (30) in section 3 explicate the function.

In deriving the T_B function, accuracy is our main concern. A model error is calculated by comparing the model T_B with the brightness temperatures computed from the more precise integral formulation. This error is 0.2 K at 6.6 GHz and increases to a maximum value of 2.1 K at 37 GHz, h-pol. The error is an rms average over an ensemble of winds and atmospheres ranging from a specular surface and clear sky to a 21 m/s wind and a very heavy cloud layer containing 60 mg/cm² of liquid water. These error figures do not include any error in the specification of the wind-induced emissivity. Also we did not consider rain in the error analysis. The accuracy of the function can also be assessed by its performance in retrieving environmental parameters via least squares estimation. When compared with surface observations, the rms difference is 0.9 K in sea-surface temperature, 1.5 m/s in wind speed, and 0.3 g/cm² in water vapor [Wentz et al., 1981b, 1982]. These accuracies are for atmospheric conditions ranging from clear skies to heavy clouds and possible light rain.

In addition to deriving the T_B function, we also compare several of the model parameters with values obtained elsewhere. In particular, the rain cloud absorption coefficients derived from the SMMR data are compared with theoretical Mie coefficients. Also, the fractional sea foam coverage, the foam reflectivity, and the large-scale sea-surface slope variance are calculated from the SMMR-inferred wind-induced emissivities. These three parameters are then compared with values obtained from optical measurements, radar measurements, a sea wave spectrum, and theory. The comparisons show very good agreement, and the model provides a consistent description of the relevant physical processes.

Section 2 reviews the basic radiative transfer and scattering theory for microwave brightness temperatures. In section 3, a number of approximations are made in the theory, and the T_B model function is derived. Sections 4 and 5 provide details on the atmosphere model and the sea-surface model, respectively. Our conclusions are given in section 6.

2. Brightness Temperature Theory

In this section we derive the equation for the brightness temperature upwelling from the sea surface through the intervening atmosphere. Radiative emission and scattering by the sea surface is considered along with radiative absorption and emission by the atmosphere. However, we do not consider the radiative scattering in the atmosphere due to rain drops. Section 4 discusses the effect of rain on SMMR brightness temperatures. When rain is present, the SMMR brightness temperatures disagree with those computed from the absorption-emission approximation in which Rayleigh absorption coefficients are used. However, if Mie absorption coefficients are used, rather than Rayleigh, the computed brightness temperatures for rain are in much closer agreement with the observation. The absorption-emission approximation is given by the following differential equation:

$$\partial T_B(\mathbf{k}_i,\varepsilon)/\partial k_i = -\alpha(\mathbf{k}_i)[T_B(\mathbf{k}_i,\varepsilon) - T_a(\mathbf{k}_i)] \quad (2)$$

where $T_B(\mathbf{k}_i,\varepsilon)$ is the upwelling brightness temperature of radiation that has travelled from the sea-surface a distance $|\mathbf{k}_i| = k_i$ along the propagation vector $\mathbf{k}_i$. The radiation is in the polarization state ε, which for our consideration is either horizontal or vertical. The derivative in (2) is with respect to the path length k_i along $\mathbf{k}_i$. The absorption coefficient $\alpha(\mathbf{k}_i)$ and the air temperature $T_a(\mathbf{k}_i)$ depend on the vector $\mathbf{k}_i$ but not on polarization.

The boundary condition for (2) is that the brightness temperature at the surface $T_B(\mathbf{k}_i,\varepsilon)|_0$ equals the brightness temperature of the surface emission plus the brightness temperature of radiation scattered by the surface. The surface T_B is given by Peake [1959]

$$T_B(\mathbf{k}_i,\varepsilon)|_0 = E(\mathbf{k}_i,\varepsilon)\, T_s + (4\pi \cos\theta_i)^{-1} \int_{2\pi} d\mathbf{k}_s\, T_B(\mathbf{k}_s)|_0\, [\sigma^0(\mathbf{k}_s,\varepsilon,\mathbf{k}_i,\varepsilon) + \sigma^0(\mathbf{k}_s,\varepsilon^*,\mathbf{k}_i,\varepsilon)] \quad (3)$$

where $E(\mathbf{k}_i,\varepsilon)$ is the surface emissivity for radiation emitted in the direction $\mathbf{k}_i$ and in polarization state ε. The surface temperature is denoted by T_s. The quantity θ_i is the incidence angle between the propagation vector $\mathbf{k}_i$ and the earth radius vector $\mathbf{r}$ at the surface element being considered. The scattering integral in (3) is over all differential solid angles $d\mathbf{k}_s$ in the

upper hemisphere of 2π steradians. The quantity $T_B(\mathbf{k}_s)|_0$ is the downwelling brightness temperature at the surface coming from the differential solid angle $d\mathbf{k}_s$. This downwelling brightness temperature propagates along $\mathbf{k}_s$ and is due to unpolarized atmospheric emission and cosmic radiation. The term $\sigma^0(\mathbf{k}_s,\varepsilon,\mathbf{k}_i,\varepsilon)$ is the bistatic normalized radar cross section (NRCS) for ε polarized radiation incident along $\mathbf{k}_s$ and ε polarized radiation scattered along $\mathbf{k}_i$. The other NRCS in (3) is for scattered ε^* polarized radiation, where ε^* is the polarization state orthogonal to ε. The NRCS equals Peake's scattering coefficients times the cosine of the angle θ_s made by $-\mathbf{k}_s$ and $\mathbf{r}$. Assuming thermal equilibrium, Kirchhoff's law allows the emissivity to be expressed as an integral of the NRCS.

$$E(\mathbf{k}_i,\varepsilon) = 1 - (4\pi \cos\theta_i)^{-1} \int_{2\pi} d\mathbf{k}_s [\sigma^0(\mathbf{k}_s,\varepsilon,\mathbf{k}_i,\varepsilon) + \sigma^0(\mathbf{k}_s,\varepsilon^*,\mathbf{k}_i,\varepsilon)] \quad (4)$$

The downwelling T_B varies according to the differential equation

$$\partial T_B(\mathbf{k}_s)/\partial k_s = -\alpha(\mathbf{k}_s)[T_B(\mathbf{k}_s) - T_a(\mathbf{k}_s)] \quad (5)$$

where $T_B(\mathbf{k}_s)$ is the brightness temperature of the unpolarized radiation that has travelled from the top to the atmosphere a distance $|\mathbf{k}_s| = k_s$ along the propagation vector $\mathbf{k}_s$. As in (2), $\alpha(\mathbf{k}_s)$ and $T_a(\mathbf{k}_s)$ are the absorption coefficient and air temperature at the position specified by $\mathbf{k}_s$. The atmosphere is assumed to be horizontally uniform and extends vertically to an altitude H. The boundary condition for (5) is that the brightness temperature at the top to the atmosphere $T_B(\mathbf{k}_s)|_H$ equals the brightness temperature of the cosmic radiation T_c.

$$T_B(\mathbf{k}_s)|_H = T_c \quad (6)$$

The upwelling brightness temperature at the top of the atmosphere $T_B(\mathbf{k}_i,\varepsilon)|_H$ is found by solving the first-order differential equations (2) and (5) imposing the respective boundary conditions (3) and (6). In solving the equations we transform from path length variables k_i and k_s to the height h above the surface. This transformation requires that the absolute derivatives $|\partial k_i/\partial h|$ and $|\partial k_s/\partial h|$ be specified. Neglecting the earth curvature, which is quite valid for incidence angles less than 60° or 70°, the derivatives are

$$|\partial k_j/\partial h| = \sec\theta_j \quad (7)$$

where j = i or s.

Using (7) to solve (2) and (5) gives

$$T_B(\mathbf{k}_i,\varepsilon)|_H = \tau(\theta_i,0,H)\, T_B(\mathbf{k}_i,\varepsilon)|_0 + \int_0^H dh \sec\theta_i\, \alpha(h)\, T_a(h)\, \tau(\theta_i,h,H) \quad (8)$$

$$\tau(\theta,h_1,h_2) = \exp\Big[-\int_{h_1}^{h_2} dh \sec\theta\, \alpha(h)\Big] \quad (9)$$

The first term in (8) is the T_B component due to surface emission and scattering. This component is attenuated by the transmittance $\tau(\theta_i,0,H)$. The transmittance function given by (9) is the atmospheric transmittance for radiation traveling from h_1 to h_2 along a slant path that makes an angle θ with $\mathbf{r}$. The second term in (8) is the T_B component due to upwelling atmospheric emission. The quantities $\alpha(h)$ and $T_a(h)$ are the absorption coefficient and air temperature at a height h. The surface brightness temperature $T_B(\mathbf{k}_i,\varepsilon)|_0$ is given by (3) with the following expression for the downwelling brightness temperature:

$$T_B(\mathbf{k}_s)|_0 = \tau(\theta_s,0,H)\, T_c + \int_0^H dh \sec\theta_s\, \alpha(h)\, T_a(h)\, \tau(\theta_s,0,h) \quad (10)$$

The first term is due to the attenuated cosmic radiation, and the second term is due to the downwelling atmospheric emission.

In summary, the upwelling brightness temperature at the top of the atmosphere can be calculated from (8) and its supporting equations given the following:

1. The observation vector $\mathbf{k}_i$ and polarization state ε.
2. The earth radius vector $\mathbf{r}$.
3. The sea-surface NRCS $\sigma^0(\mathbf{k}_s,\varepsilon,\mathbf{k}_i,\varepsilon)$ and $\sigma^0(\mathbf{k}_s,\varepsilon^*,\mathbf{k}_i,\varepsilon)$.
4. The surface temperature T_s.
5. The atmospheric profiles for the absorption coefficient $\alpha(h)$ and air temperature $T_a(h)$.
6. The cosmic brightness temperature T_c.

3. Simplified Brightness Temperature Model Function

In this section we apply a number of approximations to the integral brightness temperature equation (8) and its supporting equations. Our objective is to obtain a simple equation for brightness temperature that does not contain integrals. The first approximation concerns the scattering integral in (3). This integral describes how the downwelling radiation is scattered by the rough sea surface. The scattering of microwaves by the sea surface has been the subject of many investigations. In particular, Stogryn [1967], Wu and Fung [1972], and Wentz [1975] reported on the effect that scattering has on brightness temperature. Wentz [1977] derived parametric expressions for the bistatic NRCS that appear in (3). These expressions are applicable to all incidence and scattering angles, except near grazing, and are used to numerically evaluate the scattering integral. An analysis of the numerical integrations shows that an accurate

TABLE 1. Brightness Temperature of Diffusely Scattered Atmospheric Radiation

SMMR Channel	Scattering Integral mean (K)	Scattering Integral rms (K)	Integral - I_Ω mean (K)	Integral - I_Ω rms (K)	ω (s/cm)
6.6 V	0.2	0.2	0.0	0.0	0.70×10^{-3}
6.6 H	0.4	0.5	0.0	0.1	1.18×10^{-3}
10.7 V	0.5	0.6	0.0	0.1	1.34×10^{-3}
10.7 H	1.2	1.5	0.0	0.2	2.37×10^{-3}
18 V	1.3	1.5	0.1	0.2	1.23×10^{-3}
18 H	3.6	4.2	0.2	0.7	2.33×10^{-3}
21 V	1.9	2.0	0.3	0.7	0.81×10^{-3}
21 H	6.0	6.5	0.8	1.8	1.73×10^{-3}
37 V	1.7	1.8	0.4	0.7	0.75×10^{-3}
37 H	6.2	6.6	1.1	2.4	1.82×10^{-3}

closed-form approximation to the scattering integral exists.

The closed-form approximation is obtained by noting that the sea-surface NRCS is highly directional. For a flat specular sea surface, the atmospheric radiation scattered in direction $\mathbf{k}_i$ is due solely to the reflection of downwelling radiation incident along the propagation vector $\mathbf{k}_r$

$$\mathbf{k}_r = \mathbf{k}_i - 2(\mathbf{k}_i \cdot \mathbf{r})\mathbf{r} \tag{11}$$

where $\mathbf{r}$ is the earth radius vector normalized to unit length. For a rough sea surface the downwelling radiation is scattered in a variety of directions. As a result, the power scattered in direction $\mathbf{k}_i$ is primarily due to incident power coming from a cone centered on $\mathbf{k}_r$. The width of the cone increases with surface roughness. The closed-form approximation is found by expanding the downwelling brightness temperature $T_B(\mathbf{k}_s)|_0$ about the propagation vector $\mathbf{k}_r$.

$$T_B(\mathbf{k}_s)|_0 = T_B(\mathbf{k}_r)|_0 + \Omega(\mathbf{k}_r,\mathbf{k}_s) \tag{12}$$

where $\Omega(\mathbf{k}_r,\mathbf{k}_s)$ is the variation of the downwelling brightness temperature relative to $T_B(\mathbf{k}_r)|_0$, which is given by (10) with $\mathbf{k}_r$ replacing $\mathbf{k}_s$. Substituting (12) into (3) and utilizing the relationship (4) between the emissivity and the NRCS yields

$$T_B(\mathbf{k}_i,\varepsilon)|_0 = E(\mathbf{k}_i,\varepsilon)\, T_s + [1 - E(\mathbf{k}_i,\varepsilon)]\, T_B(\mathbf{k}_r)|_0 + (4\pi \cos\theta_i)^{-1} \int_{2\pi} d\mathbf{k}_s\, \Omega(\mathbf{k}_r,\mathbf{k}_s)[\sigma^0(\mathbf{k}_s,\varepsilon,\mathbf{k}_i,\varepsilon) + \sigma^0(\mathbf{k}_s,\varepsilon^*,\mathbf{k}_i,\varepsilon)] \tag{13}$$

where the first term is the surface emission T_B, the second term is the reflected atmospheric T_B, and the integral is the diffusely scattered atmospheric T_B. The scattered component is second-order relative to the reflected component because of the following reasons. Firstly, for $\mathbf{k}_r = \mathbf{k}_s$, the NRCS is a maximum while $\Omega(\mathbf{k}_r,\mathbf{k}_s)$ is zero. Also, as $|\mathbf{k}_s - \mathbf{k}_r|$ increases from zero, the NRCS decreases rapidly relative to the slower variation of $\Omega(\mathbf{k}_r,\mathbf{k}_s)$ about zero. Finally, the NRCS is approximately an even function of the incidence angle difference $\theta_s - \theta_r$, where θ_s and θ_r are the incidence angles for $\mathbf{k}_s$ and $\mathbf{k}_r$, respectively. The term $\Omega(\mathbf{k}_r,\mathbf{k}_s)$ is approximately an odd function of $\theta_s - \theta_r$. Hence the integral of the NRCS times $\Omega(\mathbf{k}_r,\mathbf{k}_s)$ tends to be small. However, the integral is still significant and needs to be accounted for.

We numerically evaluate the scattering integral in (13) for an ensemble of wind states and atmospheric conditions. Five wind states are considered ranging in friction velocities from 20 to 100 cm/s, which corresponds to a wind speed range from 6 to 21 m/s. Ten atmospheres are considered ranging from clear skies to a very heavy cloud layer having a columnar liquid water content of 60 mg/cm^2. The scattering integration is over a large-scale sea-surface slope distribution. By 'large-scale' we mean those ocean waves having wavelengths large compared to the radiation wavelength. The slope variance $\langle S^2 \rangle$ for the distribution is given in section 5 as a function of the friction velocity U_* and SMMR frequency. The results of the numerical integrations are summarized in Table 1, which gives the ensemble mean and rms value of the scattering integral for the ten SMMR channels at an incidence angle of 49°. The table shows that diffuse scattering is a significant term in the T_B equation. At 21 and 37 GHz, h-pol, the diffuse scattering contributes 6 K to the brightness temperature.

An analysis of these results shows that the integral is approximately proportional to the friction velocity U_*, to the downwelling brightness temperature $T_B(\mathbf{k}_r)|_0$, and to the sea-surface

reflectivity $1-E(\mathbf{k}_i,\varepsilon)$. Hence, in our model we approximate the diffuse scattering integral by

$$I_\Omega = \omega\, U_*\, T_B(\mathbf{k}_r)|_0\, [1 - E(\mathbf{k}_i,\varepsilon)] \qquad (14)$$

The constant ω is found for each SMMR channel by minimizing the ensemble variance between I_Ω and the numerically evaluated integral. Table 1 gives ω along with the mean and rms residual of the integral minus I_Ω. The accuracy of the I_Ω model, as indicated by the rms residual, is a sizable improvement over the error caused by neglecting the diffuse scattering.

Equations (8), (10), (13), and (14) are combined to obtain a simpler expression for the upwelling brightness temperature measured at altitude H.

$$T_B(\mathbf{k}_i,\varepsilon)|_H = \tau(\theta_i,0,H)\,\big[E(\mathbf{k}_i,\varepsilon)\, T_s + (1+\omega U_*)[1 - E(\mathbf{k}_i,\varepsilon)]\, T_B(\mathbf{k}_r)|_0\big] + \int_0^H dh\, \sec\theta_i\, \alpha(h)\, T_a(h)\, \tau(\theta_i,h,H) \qquad (15)$$

$$T_B(\mathbf{k}_r)|_0 = \tau(\theta_i,0,H)\, T_c + \int_0^H dh\, \sec\theta_i\, \alpha(h)\, T_a(h)\, \tau(\theta_i,0,h) \qquad (16)$$

In deriving (16) we make use of the fact that the incidence angle θ_r equals θ_i by virtue of (11).

The remaining step in the simplification process is to find closed-form expressions for the atmospheric integrals appearing in (15) and (16). The absorption coefficient $\alpha(h)$ in the atmospheric integrals is the sum of the absorption coefficients for oxygen, water vapor, and liquid water

$$\alpha(h) = \alpha_o(h) + \alpha_v(h) + \alpha_l(h) \qquad (17)$$

To simplify the atmospheric integrals we note that variations in $\alpha_o(h)$, $\alpha_v(h)$, and $\alpha_l(h)$ are primarily due to variations in the density (g/cm^3) of oxygen, water vapor, and liquid, denoted by $\rho_o(h)$, $\rho_v(h)$, and $\rho_l(h)$, respectively. There is also a small dependence on air temperature, particularly for liquid water. Factoring out a density and a temperature dependence gives

$$\alpha(h) = \rho_o(h)\, \gamma_o[T_a(h)]\, \bar{\alpha}_o + \rho_v(h)\, \gamma_v[T_a(h)]\, \bar{\alpha}_v + \rho_l(h)\, \gamma_l[T_a(h)]\, \bar{\alpha}_l \qquad (18)$$

$$\gamma_j[T_a(h)] = 1 + Q_j[T_a(h) - \langle T_j^e\rangle]\ ,\ j = o,v,l \qquad (19)$$

The air temperature function given by (19) accounts for most of the air temperature dependence in the absorption coefficients. The function is referenced to the ensemble-average effective temperature of oxygen, water vapor, and liquid water, denoted by $\langle T_o^e\rangle$, $\langle T_v^e\rangle$, and $\langle T_l^e\rangle$, respectively. The effective temperature is defined as a weighted average of the air temperature over the vertical extent of the constituent. The average is weighted by the density of the constituent.

$$T_j^e = \int_0^H dh\, \rho_j(h)\, T_a(h) \;/\; \int_0^H dh\, \rho_j(h) \qquad (20)$$

The ensemble average $\langle T_j^e\rangle$ is found by averaging T_j^e over the ensemble of 609 atmospheres described in section 4. This averaging gives values of 253 K, 279 K, and 275 K for oxygen, water vapor, and liquid water, respectively. The quantities $\bar{\alpha}_o$, $\bar{\alpha}_v$, and $\bar{\alpha}_l$ are called the normalized absorption coefficients. They have a very small dependence on air temperature, air pressure, and, in the case of $\bar{\alpha}_v$, on density $\rho_v(h)$. In our model they are assumed constants. This assumption is accurate except for a rain cloud. In this case Mie scattering becomes important, and $\bar{\alpha}_l$ also depends on the rain drop size distribution. Section 4 discusses the rain cloud case and derives values for the temperature sensitivities Q_j and the normalized absorption coefficients $\bar{\alpha}_j$.

Under the assumption that $\bar{\alpha}_j$ is constant, the transmittance $\tau(\theta_i,0,H)$ given by integral (9) can be solved in terms of the effective temperature given by (20).

$$\tau(\theta_i,0,H) = \exp\,[-\sec\theta_i(\bar{\alpha}_o\gamma_o 0_2 + \bar{\alpha}_v\gamma_v V + \bar{\alpha}_l\gamma_l L)] \qquad (21)$$

$$\gamma_j = 1 + Q_j[T_j^e - \langle T_j^e\rangle] \qquad (22)$$

The columnar contents (g/cm^2) of oxygen, water vapor, and liquid water, denoted by 0_2, V, and L in (21), are given by

$$C_j = \int_0^H dh\, \rho_j(h) \qquad (23)$$

In our model the effective temperatures T_j^e are calculated from

$$T_j^e = T_a - \langle T_a - T_j^e\rangle \qquad (24)$$

where T_a is the surface air temperature, which is a model variable, and $\langle T_a - T_j^e\rangle$ is the average difference between the surface air temperature and the effective temperature. The ensemble averages $\langle T_a - T_j^e\rangle$ for the 609 atmospheres are 36 K, 10 K, and 14 K for oxygen, vapor, and liquid, respectively.

In order to find a closed-form solution to the remaining atmospheric integrals, we approximate the density altitude variation in (18) by a unit step function denoted by $u(\cdots)$

$$\rho_j(h) = (C_j/H_e)\, u(H_e - h) \qquad (25)$$

In (25), H_e is the effective height of the atmosphere. Section 4 describes the derivation of H_e, which is a constant for a given frequency. The temperature function $\gamma_j(\cdots)$ in (18) is approximated by its effective value given by (22). One other approximation is required before the atmospheric integrals can be solved. The air temperature $T_a(h)$ in (15) and (16) is assumed to decrease linearly with h.

$$T_a(h) = T_a - \lambda h \tag{26}$$

where T_a is the air temperature at the surface and λ is the lapse rate taken to be 5.9 K/km, which is the average value for the 609 atmospheres. The accuracy of these approximations is determined in section 4 by comparing the T_B's calculated from this approximate formulation with the T_B's calculated by numerically integrating the T_B equation.

Equation (18) with the above three approximations is substituted into equations (15) and (16), and the atmospheric integrals are solved. The result is the desired brightness temperature model function:

$$T_B(\mathbf{k}_i,\varepsilon)|_H \sim f(T_s,U_*,V,L,T_a) =$$

$$\tau\left[ET_s + (1+\omega U_*)(1-E)[(1-\tau)(T_a-\lambda d) + \tau T_c]\right]$$

$$+ (1-\tau)[T_a - \lambda(H_e-d)] \tag{27}$$

$$\tau = \exp[-\sec\theta_i(\bar{\alpha}_o\gamma_o O_2 + \bar{\alpha}_v\gamma_v V + \bar{\alpha}_1\gamma_1 L)] \tag{28}$$

$$d = H_e[(\tau - 1 - \tau\ln\tau)/(1n\ \tau - \tau\ 1n\ \tau)] \tag{29}$$

$$\gamma_j = 1 + Q_j(T_a - \langle T_a\rangle)\ ,\ j = o,\ v,\ 1 \tag{30}$$

The three supporting equations give the atmospheric transmittance τ, the effective emission depth d for the atmosphere, and the air temperature coefficient γ_j. The emission depth d equals $H_e/2$ when τ equals unity. As τ goes to zero for highly attenuating atmospheres, the emission depth tends to the limit $-H_e/\ln\tau$, which equals the power penetration depth. The average global air temperature $\langle T_a\rangle$ and lapse rate λ are taken to be 289 K and 5.9 K/km based on the ensemble average of the 609 atmospheres. The upwelling and downwelling atmospheric brightness temperature components are given by $(1-\tau)[T_a-\lambda(H_e-d)]$ and $(1-\tau)(T_a-\lambda d)$, respectively. The term τT_c is the attenuated cosmic radiation incident onto the sea surface, with T_c= 2.76 K. The factor $1+\omega U_*$ accounts for the diffuse scattering of atmospheric radiation from the sea-surface. The quantities O_2, V, and L are the columnar contents (g/cm^2) for oxygen, water vapor, and liquid water. The columnar water vapor and liquid water are model funcion variables, whereas O_2 is assumed constant because the global variation of oxygen attenuation is negligably small at the SMMR frequencies. The other model function variables are the sea-surface temperature T_s, the friction velocity U_*, and the surface air temperature T_a. The sea-surface emissivity, denoted simply as E in (27), is a function of T_s and U_* given by equations (35), and (38) through (42) in section 5. Values for all of the model function constants are contained in this paper.

The interpretation of the columnar liquid water content L needs some explanation. We assume that the normalized absorption coefficient for liquid water is constant for a given frequency. When there is no rain in the field of view, $\bar{\alpha}_1$ is indeed constant, equaling the Rayleigh value. In this case, L is an accurate measure of the columnar liquid water content. However, for rain clouds, $\bar{\alpha}_1$ varies considerably due to the rain drop size distribution. For these high attenuation cases, the quantity L becomes a relative indicator of liquid water absorption rather than an absolute measure of the columnar liquid water. For this reason, we refer to it as the 'effective' liquid water content.

4. Atmosphere Model

In this section we determine values for the following atmospheric parameters: temperature sensitivities Q_o, Q_v, and Q_1, oxygen opacity $\bar{\alpha}_o O_2$, water vapor and liquid water normalized absorption coefficients $\bar{\alpha}_v$ and $\bar{\alpha}_1$, and effective columnar height H_e. For each SMMR frequency, the temperature sensitivities are found from least squares fits of the absorption coefficients versus temperature. The parameters $\bar{\alpha}_o O_2$, $\bar{\alpha}_v$, and $\bar{\alpha}_1$ are determined so as to minimize the variance between the model function transmittance (28) and the more precise transmittance given by the integral equation (9). Unlike the columnar water vapor V and liquid water L, the columnar oxygen O_2 is essentially constant, and it is more convenient to work with the product of O_2 times $\bar{\alpha}_o$, rather than $\bar{\alpha}_o$ separately. An effective columnar height H_e is found for each frequency by minimizing the variance between the model function T_B (27) and the more accurate T_B given by (8). The variance minimizations are done over an ensemble of 609 different atmospheric profiles derived from radiosonde flights and surface observatons of cloud type and coverage. The profiles exclude rain, and as a result the estimated $\bar{\alpha}_1$ correspond to the Rayleigh absorption coefficients. The final step in estimating the atmospheric parameters is to adjust $\bar{\alpha}_1$ in order to account for Mie scattering from rain drops. This adjustment is based on SMMR observations of rain clouds.

According to (19) the temperature dependence of the absorption coefficients is modeled by

$$\alpha_j(T) = [1 + Q_j(T - \langle T_j^e\rangle)]\ \alpha_j(\langle T_j^e\rangle)\ ,$$

$$j = o,v,1 \tag{31}$$

where T is the temperature of the constituent and $\langle T_j^e\rangle$ is the ensemble-average effective tempera-

TABLE 2. Temperature Sensitivities of Absorption Coefficients

Frequency (GHz)	Oxygen, Q_o (K^{-1})	Vapor, Q_v (K^{-1})	Liquid, Q_l (K^{-1})
6.6	-1.14×10^{-2}	-0.65×10^{-2}	-2.85×10^{-2}
10.7	-1.14×10^{-2}	-0.61×10^{-2}	-2.82×10^{-2}
18	-1.14×10^{-2}	-0.36×10^{-2}	-2.73×10^{-2}
21	-1.13×10^{-2}	-0.06×10^{-2}	-2.68×10^{-2}
37	-1.11×10^{-2}	-0.65×10^{-2}	-2.33×10^{-2}

ture given in section 3. The temperature sensitivities Q_j are found for each frequency from a least squares fit of (31) to the actual absorption coefficients $\alpha_j(T)$. The fit is over temperatures T ranging from $\langle T_j^e \rangle$ - 20 K to $\langle T_j^e \rangle$ + 20 K in 1 K steps. The oxygen coefficient $\alpha_o(T)$ is computed according to Meeks and Lilley [1963]. The water vapor coefficient $\alpha_v(T)$ is computed using the expressions given by Barrett and Chung [1962]. The Rayleigh scattering approximation [Goldstein, 1951] is used to calculate the liquid water coefficient $\alpha_l(T)$. In these calculations we let the air pressure be 635 and 900 mb for oxygen and water vapor, respectively. The water vapor density is taken to be 10 g/m³. Note that the temperature sensitivity is essentially independent of these choices for air pressure and water vapor density. The values for Q_j are shown in Table 2 for the 5 SMMR frequencies. The liquid water absorption is most sensitive to temperature changes, the oxygen absorption is moderately sensitive, and the waper vapor absorption is nearly independent of temperature.

The oxygen opacity $\bar{\alpha}_o O_2$ and the normalized absorption coefficients $\bar{\alpha}_v$ and $\bar{\alpha}_l$ are found by minimizing over an ensemble of atmospheres the variance between the closed-form model function transmittance (28) and the transmittance given by the more exact integral equation (9). The ensemble of atmospheres is 609 profiles of temperature, pressure, and water vapor measured by radiosondes. In addition, surface observations of cloud types and coverage at the time of the radiosonde flights are used to specified liquid water profiles. These data are for the entire year of 1972 at three islands: Jan Mayen (subarctic), the Azores (temperate), and Truk (tropics). The 609 atmospheres are representative of the seasonal and regional variations experienced by an orbiting radiometer except that rainy days are excluded. Also profiles having a liquid water content exceeding 60 mg/cm² are excluded. The technique for constructing the profiles from the observed data is reported by Wentz and Stumpf [1978]. For each radiosonde level in a given profile, the absorption coefficients for the oxygen, water vapor, and liquid water are computed according to the references given in the preceding paragraph. The three absorption coefficients are summed to obtain the total absorption coefficient $\alpha(h)$, and the integrated radiative transfer equation (9) is then used to computed the transmittance. A SMMR incidence angle of 49° is assumed for these computations. The transmittance model function uses the columnar water vapor V, the columnar liquid water L, and the surface air temperature T_a rather than discrete profiles. The two columnar contents in terms of g/cm² are found by integrating the radiosonde water vapor and liquid water profiles according to (23). The air temperature comes from the surface observations. Having specified V, L, and T_a, the only unknowns in transmittance model function are $\bar{\alpha}_o O_2$, $\bar{\alpha}_v$, and $\bar{\alpha}_l$. These unknowns are determined by minimizing the variance between the 609 transmittances computed from (9) and the transmittances computed from the transmittance model function (28). Table 3 gives their values for the five SMMR channels. The values for $\bar{\alpha}_l$ are labeled 'Rayleigh' to indicate that they apply to small cloud droplets, but not rain drops.

The one remaining atmospheric parameter to be specified is the effective height H_e. This parameter is found in a manner analogous to that described in the preceding paragraph. The integrated radiative transfer equation (8) is used to compute brightness temperatures. A h-pol and v-pol T_B at an incidence angle of 49° are computed for each profile, giving a total of 1218 brightness temperatures. In these computations we assume a specular sea surface at a temperature T_s that is typical for the island and month under consideration. In section 5, (38) gives the specular sea-surface emissivity E_s as a function of temperature T_s. The unknown model function parameter H_e is found by minimizing the variance between the 1218 T_B's computed from integral equation (8) and the T_B's computed from the model function (27). The values of H_e for the five SMMR frequencies are given in Table 3 along with the rms residual ΔT_B between the model function T_B and the T_B computed from (8). At the higher frequencies water vapor and liquid water are the dominate absorption mechanisms. Since the bulk of the water vapor and liquid water is at an altitude lower than that of oxygen, the effective height is less at the higher frequencies. The

TABLE 3. Atmospheric Absorption Coefficients, Effective Height, and Model Error

	Opacity	Normalized Absorption Coefficients				
Frequency (GHz)	Oxygen, $\bar{\alpha}_o O_2$ (millinapers)	Vapor, $\bar{\alpha}_v$ $\frac{\text{millinapers}}{\text{g/cm}^2}$	Rayleigh, $\bar{\alpha}_1$ $\frac{\text{millinapers}}{\text{mg/cm}^2}$	SMMR, $\bar{\alpha}_1$ $\frac{\text{millinapers}}{\text{mg/cm}^2}$	Effective Height H_e (km)	Model Error ΔT_B (K)
6.6	8.29	1.05	0.078	0.112	7.4	0.19
10.7	8.59	2.47	0.200	0.401	6.0	0.28
18	9.72	13.62	0.562	1.125	4.4	0.63
21	10.78	45.45	0.741	1.360	4.5	0.70
37	29.04	23.90	2.224	2.224	4.5	1.15

rms residual ΔT_B given in Table 3 is a measure of the atmosphere model accuracy as compared to the integrated radiative transfer equation. The model accuracy is 0.2 K at 6.6 GHz and gradually degrades to 1.1 K at 37 GHz.

The final step in estimating the atmospheric parameters is to adjust the liquid water coefficients $\bar{\alpha}_1$ to account for Mie scattering from rain drops. This adjustment corrects three problems that occur when the Rayleigh coefficients given in Table 3 are used to retrieve environmental parameters. The first problem is that the columnar liquid water L inferred from the 18 GHz channels is twice as large as that inferred from the 37 GHz channels. This inconsistency is graphically shown in Figure 1. The vertical axes is the columnar liquid water retrieved by SMMR geophysical algorithm [Wentz et al., 1981b], when the 37 GHz channels are not used. The horizontal axes is the liquid water retrieved when the 18 GHz channels are not used. The 102 points in the figure correspond to 50 km resolution cells in the vicinity of Hurricane Ella during SEASAT rev. 952. The least squares fit, shown by the straight line, has a slope of about 2 rather than unity. Similar scatter plots for Hurricane Fico and for the Intertropical Convergence Zone show that L inferred from 18 GHz is consistently twice as large as that inferred from 37 GHz. From these plots we conclude that the ratio of the 37 GHz to 18 GHz Rayleigh absorption coefficient is a factor of 2 too large for rain clouds. To correct this, we multiply the 18 GHz $\bar{\alpha}_1$ value appearing in Table 3 by a factor of 2. Also the 21 GHz $\bar{\alpha}_1$ is increased based on an interpolation between the modified 18 GHz $\bar{\alpha}_1$ and the 37 GHz $\bar{\alpha}_1$. Reprocessing the SMMR T_B's using the modified 18 and 21 GHz $\bar{\alpha}_1$ yields consistent liquid water contents. The modified 18 and 21 GHz $\bar{\alpha}_1$ are shown in Table 3 under the column labeled 'SMMR' to indicate that they are derived from SMMR measurements of rain clouds. Instead of increasing the 18 GHz $\bar{\alpha}_1$, we could have halfed the 37 GHz $\bar{\alpha}_1$. The resulting liquid water contents would still be consistent but their values would be twice as large. We decided to modify the 18 GHz $\bar{\alpha}_1$ rather than the 37 GHz $\bar{\alpha}_1$ so that the 37 GHz $\bar{\alpha}_1$ would remain equal to the Rayleigh value, which is correct for clouds without rain. When there is no rain in the field of view, the attenuation is relatively light, and the 37 GHz channels dominate in the retrieval of liquid water. For this case the retrieved value for L will be correct because the 37 GHz $\bar{\alpha}_1$ equals the Rayleigh coefficient. However, for rain clouds, as is discussed at the end of section 3, L becomes a relative indicator of liquid water atten-

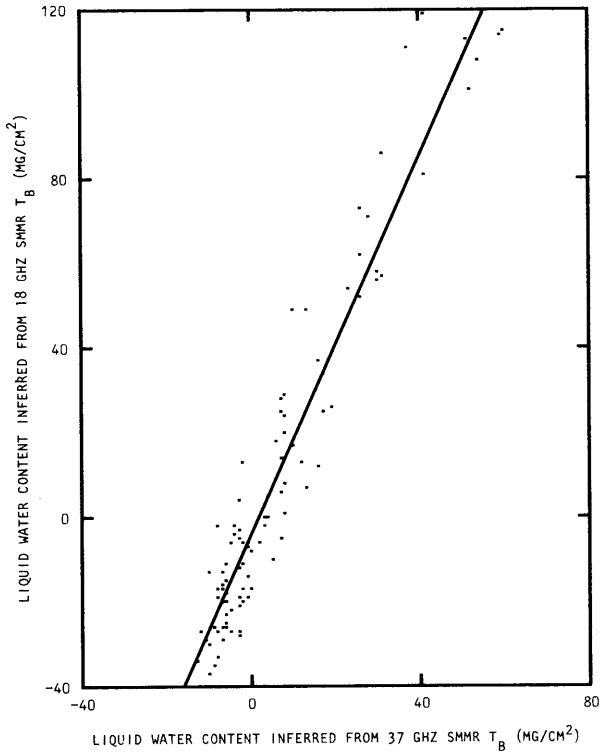

Fig. 1. A comparison of the different atmospheric liquid water contents obtained from the 18 GHz and 37 GHz SMMR channels using Rayleigh absorption coefficients.

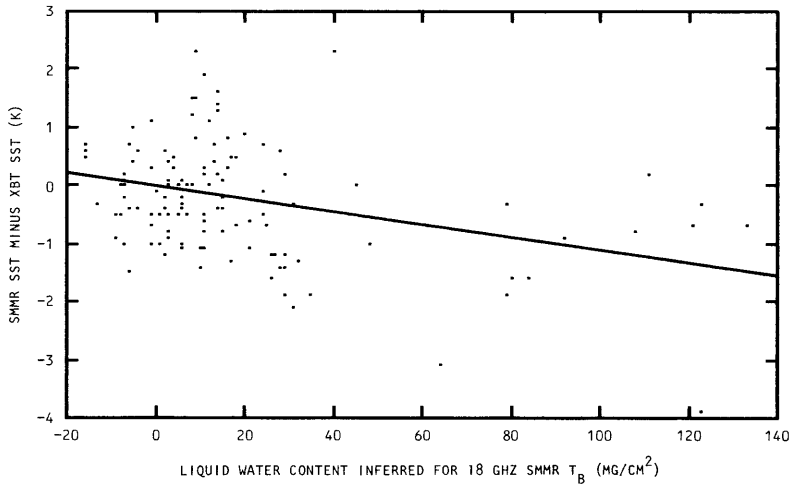

Fig. 2. The correlation between the SMMR-inferred sea-surface temperature and the SMMR-inferred liquid water contents caused by using Rayleigh absorption coefficients.

uation rather than an absolute measure of columnar liquid water.

The second problem with the Rayleigh coefficients is shown in Figure 2, in which the error in the retrieved sea-surface temperature (SST) is plotted versus the retrieved liquid water. The SST error is the SST retrieved by the SMMR geophysical algorithm minus the value measured by expendable bathythermographs (XBT). The liquid water contents are based on the 18 GHz Rayleigh coefficients. The 121 SMMR verus XBT comparisons cover the North and Tropical Pacific during the 3 month life of SEASAT. Although there is considerable scatter in the data, the figure shows a small negative correlation between the SST error and the SMMR-inferred liquid water. The least squares fit, shown by the straight line, has a slope of -0.0112 K/(mg/cm²). This correlation indicates that the SST retrieval algorithm is overcompensating for liquid water because the Rayleigh absorption coefficient at 6.6 GHz is too large compared to the 18 GHz value. We eliminate this correlation by subtracting an amount $\Delta\bar{\alpha}_1$= 0.022 from the 6.6 GHz Rayleigh $\bar{\alpha}_1$ appearing in Table 3, where

$$\Delta\bar{\alpha}_1 = [(\partial T_B/\partial T_s)/(\partial T_B/\partial\bar{\alpha}_1)]\ \Delta T_s \qquad (32)$$

The partial derivatives are computed from the 6.6 GHz, v-pol T_B model function (27) assuming a liquid water content of 100 mg/cm², and ΔT_s is the 1.12 K SST error that occurs at 100 mg/cm². The 6.6 GHz, v-pol channel is used because it is the most influential channel in retrieving SST. The correction given by (32) provides the correct 6.6 to 18 GHz absorption ratio assuming the Rayleigh value for 18 GHz. Since the 18 GHz Rayleigh coefficient is multiplied by 2 to obtain consistent liquid waters, the corrected 6.6 GHz coefficient must also be multiplied by 2 to preserve the proper 6.6 to 18 GHz ratio. The SST's retrieved using this modified 6.6 GHz $\bar{\alpha}_1$ show no correlation with liquid water.

The third problem caused by the Rayleigh coefficients is that a positive correlation between the SMMR-inferred wind speed and liquid water occurs. This correlation is eliminated by simply doubling the 10.7 GHz Rayleigh coefficient, as was done for the 18 GHz coefficient.

In Figure 3 the ratio of $\bar{\alpha}_1$ at a given frequency to the 37 GHz $\bar{\alpha}_1$ is plotted versus frequency. The values of $\bar{\alpha}_1/\bar{\alpha}_1(37)$ for the Rayleigh coefficients and for the SMMR-inferred coefficients are shown by the circles and the crosses, respectively. The solid curve in the figure is a theoretical absorption ratio for Mie scattering in a rain cloud [Tsang et al., 1977]. In computing the theoretical ratio, the Mie absorption coefficient is averaged over an ensemble of cloud

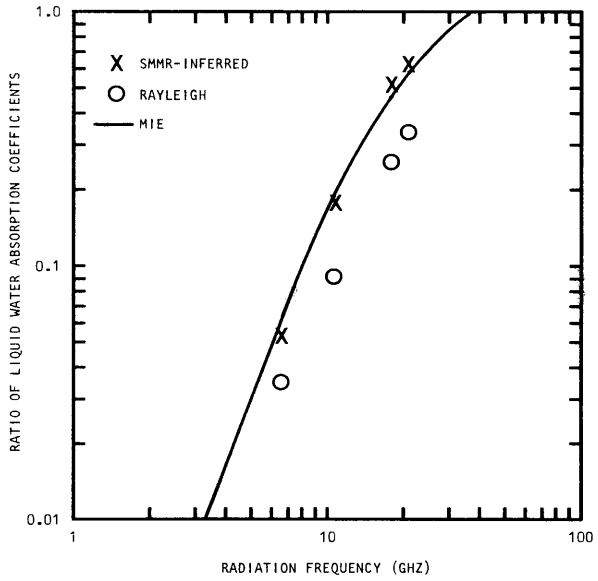

Fig. 3. A comparison of the frequency ratio for the liquid water absorption coefficients obtained from Rayleigh scattering theory, Mie scattering theory, and SMMR observations.

TABLE 4. Regression Coefficients for Specular Brightness Temperature

SMMR Channel	s_0 (K)	s_1	s_2 (K^{-1})	s_3 (K^{-2})	s_4 (K/deg)
6.6 V	1.3759×10^{2}	2.368×10^{-1}	1.565×10^{-2}	-2.311×10^{-4}	2.03
6.6 H	0.7107×10^{2}	0.891×10^{-1}	1.000×10^{-2}	-1.476×10^{-4}	-1.28
10.7 V	1.4452×10^{2}	-0.336×10^{-1}	2.076×10^{-2}	-2.497×10^{-4}	2.05
10.7 H	0.7559×10^{2}	-0.935×10^{-1}	1.371×10^{-2}	-1.661×10^{-4}	-1.32
18 V	1.5750×10^{2}	-3.936×10^{-1}	2.285×10^{-2}	-2.048×10^{-4}	2.08
18 H	0.8444×10^{2}	-3.675×10^{-1}	1.657×10^{-2}	-1.568×10^{-4}	-1.40
21 V	1.6252×10^{2}	-4.916×10^{-1}	2.237×10^{-2}	-1.775×10^{-4}	2.10
21 H	0.8802×10^{2}	-4.546×10^{-1}	1.699×10^{-2}	-1.477×10^{-4}	-1.43
37 V	1.8493×10^{2}	-7.405×10^{-1}	1.694×10^{-2}	-0.539×10^{-4}	2.11
37 H	1.0524×10^{2}	-7.666×10^{-1}	1.718×10^{-2}	-1.033×10^{-4}	-1.59

and rain drops having a drop radii distribution typical of a 12 mm/h rain [Deirmendjian, 1969]. The Mie coefficients differ from the Rayleigh coefficients because radiative scattering becomes significant for the larger rain drops. The ratios of modified coefficients coming from the SMMR data are in excellent agreement with the Mie ratios. Based on this agreement we make the following conclusion. If the emission-absorption radiative transfer equation (2), which neglects the scattering integral, is used to model a rain cloud, then Mie absorption coefficients, rather than Rayleigh, should be used.

It is also interesting to note that rain partially filling the field of view could also be responsible for the non-Rayleigh spectral brightness temperature signature observed by the SMMR. In any case, it is necessary to modify the Rayleigh coefficients in order to have the model accurately represent the observations.

5. Sea-Surface Emissivity Model

The sea surface is modeled as a composite of foam-free rough water and foam patches. The fractional area of the foam patches is denoted by F. The total sea-surface emissivity E is an area-weighted sum of the emissivity E_r for the rough water and the emissivity E_f for the foam.

$$E = (1 - F)E_r + F\,E_f \tag{33}$$

The rough water emissivity is given by

$$E_r = E_s + \Delta E_r \tag{34}$$

where E_s is the emissivity for a specular water surface and ΔE_r is the change in emissivity due to roughness. Combining (33) and (34), one obtains

$$E = E_s + \Delta E \tag{35}$$

$$\Delta E = \Delta E_r + F(E_f - E_r) \tag{36}$$

where ΔE is the total change in emissivity due to both roughness and foam. Equation (35) is used in the T_B model function (27). As is discussed below, the specular emissivity E_s is computed from a model given by Klein and Swift [1977], and the expressions for the emissivity change ΔE are found by regressing SMMR-inferred emissivities with the friction velocities measured by the SEASAT microwave scatterometer SASS [Wentz et al., 1981a].

The specular emissivity is a function of the observation frequency, polarization, and incidence angle θ_i as well as the sea-surface temperature and salinity. The frequencies we consider are 6.6 GHz and higher, and the salinity dependence is small. For example, in the open ocean the salinity varies from about 32 to 37 °/oo. This salinity variation translates into a specular T_B variation of about ± 0.1 K or less. Hence we simply assume a nominal value of 34 °/oo for all computations. To compute E_s, we use the Klein and Swift [1977] equations for the sea-water dielectric constant ε, which is a function of frequency, sea-surface temperature, and salinity. The following Fresnel equation relates the specular emissivity to the dielectric constant:

$$E_s = 1 - \left| \frac{\eta \cos\theta_i - (\varepsilon - \sin^2\theta_i)^{.5}}{\eta \cos\theta_i + (\varepsilon - \sin^2\theta_i)^{.5}} \right|^2 \tag{37}$$

where the parameter η equals unity for h-pol and equals ε for v-pol. In order to reduce computation time for the T_B model function, we find the following regression to the dielectric constant and Fresnel equations:

$$E_s T_s = s_0 + s_1 T + s_2 T^2 + s_3 T^3 + s_4(\theta_i - 49^\circ) \tag{38}$$

where $T = T_s - 273.16$. The regression only applies to the SMMR incidence angle range of $49^\circ \pm 0.5^\circ$. The s coefficients are found by fitting (38) in a least squares sense to the values given by the Fresnel equation and are shown in Table 4 for each SMMR channel. Differences between the spec-

TABLE 5. Regression Coefficients for Wind-Induced Emissivity

SMMR Channel	b (s/cm deg)	m_1 (s/cm)	m_2 (s/cm)	M_1 (s/cm)
6.6 V	-0.94×10^{-5}	1.55×10^{-4}	4.90×10^{-4}	-0.35×10^{-4}
6.6 H	0.88×10^{-5}	4.58×10^{-4}	6.02×10^{-4}	0.79×10^{-4}
10.7 V	-1.34×10^{-5}	1.41×10^{-4}	4.61×10^{-4}	-0.43×10^{-4}
10.7 H	1.39×10^{-5}	5.16×10^{-4}	7.09×10^{-4}	1.73×10^{-4}
18 V	-1.68×10^{-5}	2.66×10^{-4}	2.66×10^{-4}	-0.64×10^{-4}
18 H	1.63×10^{-5}	7.05×10^{-4}	7.05×10^{-4}	2.20×10^{-4}
21 V	-1.79×10^{-5}	2.68×10^{-4}	2.68×10^{-4}	-0.74×10^{-4}
21 H	1.82×10^{-5}	7.60×10^{-4}	7.60×10^{-4}	2.58×10^{-4}
37 V	-2.54×10^{-5}	2.80×10^{-4}	2.80×10^{-4}	-1.54×10^{-4}
37 H	2.24×10^{-5}	10.51×10^{-4}	10.51×10^{-4}	3.77×10^{-4}

ular brightness temperature $E_s T_s$ given by (38) and that given by the Fresnel equation are less than 0.1 K.

The change in emissivity ΔE due to roughness and foam is found by collocating SMMR and SASS measurements. The SMMR T_B's and the SASS normalized radar cross sections (NRCS) are collocated into 150 by 150 km cells for two North Pacific SEASAT passes (revs. 1120 and 1135). For each cell the SASS NRCS's are converted to a friction velocity U_* [Jones et al., 1982], and the SMMR T_B's are converted to an emissivity. To obtain ΔE, we subtract the specular emissivity from the SMMR-inferred emissivity. The ΔE values are then regressed versus the SASS-inferred friction velocities.

The SMMR-inferred emissivities E are found by inverting the T_B model function (27) such that E is expressed in terms of the SMMR T_B measurement, the SASS-inferred U_*, the sea-surface temperature T_s, the water vapor V, and the liquid water L. The air temperature variable T_a in the model function is set equal to T_s. Values for T_s come from the National Marine Fishery Service (NMFS) SST map for the Northeast Pacific during September 1978. Comparisons of the NMFS SST's with buoy and ship observations indicate that the map is accurate to about ± 1 C for the time and region being considered. A histogram technique is used to identify SMMR cells that are free of clouds [Wentz et al., 1981a]. In computing E, we only use these clear sky cells for which L is set to zero. The actual liquid water comtamination in these cells probably does not exceed 3 mg/cm^2. To determine the water vapor, the T_B model function is initialized using the NMFS SST, the SASS U_*, and zero liquid water. Then the water vapor for the model function is incremented upward from zero until the model function T_B equals the SMMR 21 GHz, v-pol measurement. In calculating the model function for 21 GHz, v-pol, we assume that ΔE increases linearly with U_*, having a slope of 2.9×10^{-4} s/cm. This slope agrees well with the slope finally found for 21 GHz, v-pol given in Table 5. Comparisons with radiosondes in the Gulf of Alaska indicate that these calculated water vapors for clear skies are accurate to within ± 0.2 g/cm^2 [Wentz et al., 1981b]. Having specified T_B, U_*, T_s, V, and L, we then calculate the emissivity E and change in emissivity ΔE by means of the inverted model function.

The emissivity change ΔE depends on the incidence angle θ_i. For v-pol, ΔE decreases as θ_i increases, whereas for h-pol, ΔE increases with increasing θ_i. We model this variation by

$$\Delta E = \Delta \bar{E} + b\, U_*(\theta_i - 49) \qquad (39)$$

where the $\Delta \bar{E}$ is the emissivity change at exactly 49°. The b coefficients, which are given in Table 5, are derived by numerically integrating the emissivity integral (4) for three incidence angles: 48.5°, 49.0°, and 49.5°. The variation of the integral for these three incidence angles determines the b values. The relationship between the large-scale sea-surface slope variance used in the integration and the friction velocity is discussed at the end of this section. The variation of the foam emissivity contribution $F E_f$ with θ_i is much less than the variation of the rough water contribution $(1-F)E_r$ and is set to zero when computing the b coefficients. Each SMMR-inferred ΔE is converted to a $\Delta \bar{E}$ by means of the above expression.

Figures 4 and 5 show $\Delta \bar{E}$ plotted versus U_* for v-pol and h-pol, respectively. Note that different vertical scales are used in the two figures. All SMMR frequencies are shown except 21 GHz for which the water vapor partially masks the sea-surface emissivity variations. A total of 119 cloud-free SMMR cells are found for the two North Pacific passes. The h-pol $\Delta \bar{E}$ versus U_* slope increases significantly with frequency. The v-pol slopes are nearly independent of frequency and are less steep than the h-pol slopes. This frequency and polarization behavior of the slopes is consistent with the two-scale scattering model reported by Wentz [1975]. At 6.6 and 10.7 GHz,

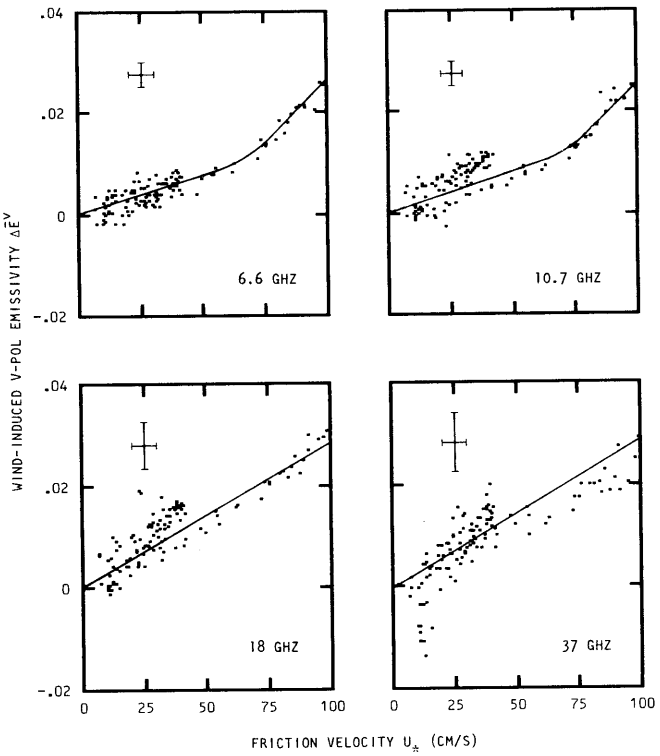

Fig. 4. The wind-induced sea-surface emissivity for vertical polarization at four SMMR frequencies.

the $\Delta\bar{E}$ versus U_* curves become steeper at the higher friction velocities. This increase in slope may be due to the onset of wave breaking at the higher wind speeds. At the higher frequencies, atmospheric contamination prohibits the possibility of seeing this nonlinear effect. The error bars in the figures indicate the uncertainty in $\Delta\bar{E}$ and U_* due to the errors in specifing T_B, T_s, U_*, V, L, and θ_i. These expected errors, which are assumed uncorrelated, are 0.4 K, 1 C, 5 cm/s, 0.2 g/cm², 1 mg/cm², and 0.1°, respectively. The emissivity error increases with frequency because of the increasing sensitivity to the atmospheric uncertainties. The solid curves in the two figures are best fits to the data. At 6.6 and 10.7 GHz, the curves are two straight lines connected by a parabola such that the curve and its first derivative are continuous. At the higher frequencies, a single straight line is fitted to the data. The equations for the best-fit curves are as follows:

$$\Delta\bar{E} = m_1 U_* \qquad U_* \leq 65 \text{ cm/s} \qquad (40)$$

$$\Delta\bar{E} = m_1 U_* + 0.05(m_2 - m_1)(U_* - 65)^2 \qquad 65 \text{ cm/s} < U_* < 75 \text{ cm/s} \qquad (41)$$

$$\Delta\bar{E} = m_2 U_* - 70(m_2 - m_1) \qquad U_* \geq 75 \text{ cm/s} \qquad (42)$$

where m_1 and m_2 are the slopes for the low and high wind speed linear segments. Table 5 gives these two slopes for the 10 SMMR channels. For the three higher channels m_1 equals m_2. The slopes for 21 GHz are obtained from a linear interpolation in frequency of the 18 and 37 GHz slopes. The above three equations along with (35), (38), and (39) provide the emissivity for the model function (27).

There are a number of secondary parameters that may affect $\Delta\bar{E}$. Firstly, $\Delta\bar{E}$ probably depends slightly on T_s. The values shown in Figures 4 and 5 are for an SST range from 12 C to 28 C. Furthermore, geometric optics predicts that $\Delta\bar{E}$ should depend on the direction of the wind relative to the observation azimuth direction. For a 20 m/s wind, at an incidence angle of 49°, and for v-pol, the theory predicts that the increase in T_B due to surface roughness is about 1 K larger when viewed in the upwind direction than when viewed in the crosswind direction. For h-pol, the upwind T_B increase is about 0.3 K less than the crosswind value. This upwind-crosswind difference is based on Cox and Munk [1954] observation that the upwind sea-surface slope variance is about 34% greater than the crosswind slope variance. Another parameter that is not considered is the fetch of the wind, which can affect the foam coverage. The dependence of $\Delta\bar{E}$ on these secondary parameters has yet to be observed experimentally, and we do not attempt to model them. However, they may contribute to some of

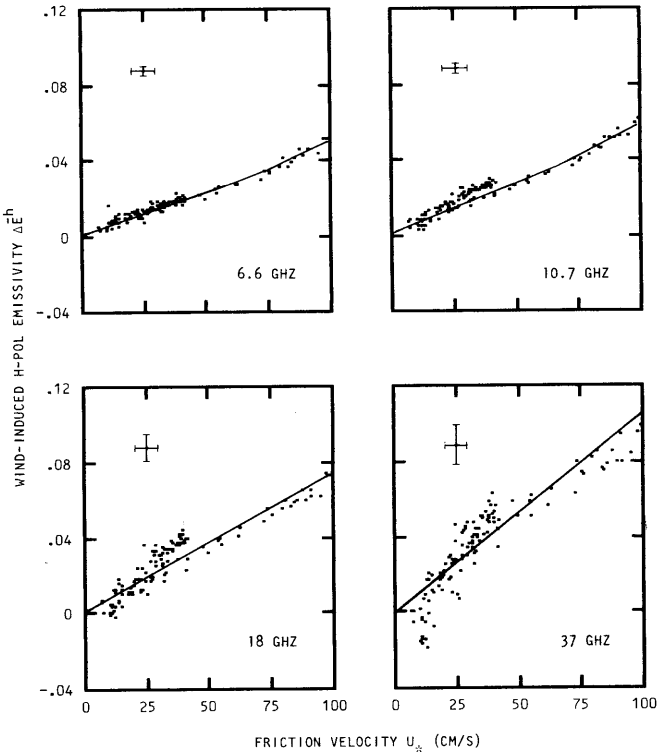

Fig. 5. The wind-induced sea-surface emissivity for horizontal polarization at four SMMR frequencies.

the data scatter shown in Figures 4 and 5.

We next consider the fractional area F of foam coverage. The emissivity integral (4) is used to remove the rough-water contribution from the SMMR-inferred emissivities, thereby leaving only the foam contribution. Equation (33) can be rewritten as

$$R = (1 - F_e)\, R_r \tag{43}$$

$$F_e = F(1 - R_f/R_r) \tag{44}$$

where R, R_r, and R_f are the reflectivities of the total sea surface, the rough water, and the foam, respectively. These reflectivities are simply one minus the corresponding emissivities. The term F_e is the effective fractional foam coverage. If the reflectivity of foam were zero, then F_e would be the actual fractional foam coverage. The effective coverage can be calculated by inverting (43)

$$F_e = (R_r - R)/R_r \tag{45}$$

in which the total refectivity R is given by

$$R = 1 - E_s - \Delta\bar{E} \tag{46}$$

where E_s comes from (38) and $\Delta\bar{E}$ comes from (40), (41), and (42). The reflectivity R_r of rough water is theoretically computed from (4) assuming an incidence angle of 49° and a sea-surface temperature of 290 K. The computed R_r is then regressed versus friction velocity to obtain

$$R_r = R_s - M_1 U_* \tag{47}$$

where R_s is the specular reflectivity. The regression coefficients M_1 appear in Table 5 for each SMMR channel.

The solid curves in Figure 6 show the effective foam coverage computed from (45) through (47) plotted versus friction velocity. Three curves are shown: the average F_e for 6.6 and 10.7 GHz, F_e for 18 GHz, and F_e for 37 GHz. Each curve is an average of h-pol and v-pol. The values computed for F_e are nearly independent of polarization. For a given frequency, the typical difference between the fractional coverage inferred from v-pol and that inferred from h-pol is only 0.005. This close agreement indicates that the ratio R_f/R_r is independent of polarization. Furthermore the F_e for 6.6 GHz differs from the 10.7 GHz values by 0.002 or less. The figure shows that F_e increases at the higher frequencies. This increase implies that R_f/R_r becomes smaller at the higher frequencies. Hence the 37 GHz curve should correspond most closely to the actual fractional foam coverage. Also in Figure 6 is the foam coverage that was deduced from photographic observations of foam [Ross and Cardone, 1974]. The crosses denote the whitecap coverage and the triangles denote the whitecap plus streak coverage. The standard deviation of

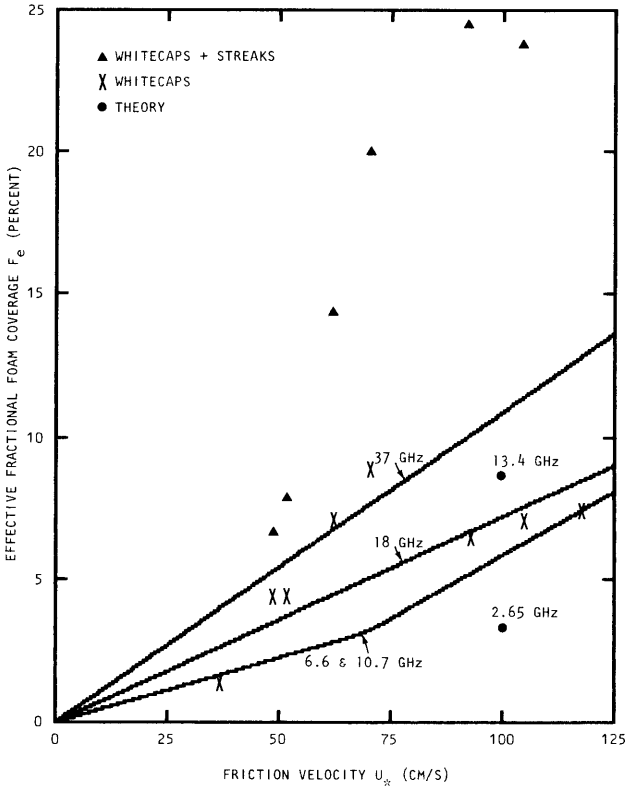

Fig. 6. A comparison of the sea-surface effective foam coverage obtained from the SMMR data, from photographic measurements, and from a dielectric layer theory.

the photographic measurements is about ±5%. The SMMR-inferred F_e corresponds more closely to the whitecap coverage, indicating that it is the whitecaps rather than the streaks that affect the sea-surface emissivity. The aircraft T_B measurements reported by Webster et al. [1976] showed no appreciable variation as the streak coverage dropped from 40% to 5%. Meanwhile, the whitecap coverage was about 4% and showed no systematic variation. These aircraft observations are another indication that streaks do not significantly alter the sea-surface emissivity. This conclusion disagress with Webster's statement that the thin streaks are the most important part of the white water signature.

Wentz [1974] theoretically computed the reflectivity of a layer of foam on top of a specular sea-surface. The foam-water surface was modeled as a layered dielectric media [Brekhovskikh, 1960]. The computations were done for a 3 cm thick foam layer at 2.65 GHz and 13.4 GHz. At the lower frequency the theoretical reflectivity ratio R_f/R_r was 0.71 and 0.68 for v-pol and h-pol, respectively. The 13.4 GHz the ratios were 0.19 and 0.20. Hence the theory agrees with the above observation that the ratio is essentially independent of polarization. Furthermore, the theory correctly predicts that the ratio decreases with frequency. The effective foam coverage at 100 cm/s is calculated from these theoretical reflectivity ratios using (44) and is

shown in Figure 6 by the two solid circles, one for 2.65 GHz and the other for 13.4 GHz. To calculate these two values, we set the actual foam coverage F equal to the effective coverage F_e at 37 GHz. The two theoretical values are in reasonable agreement with the SMMR-inferred values.

As mentioned previously, the evaluation of the emissivity integral (4) and the scattering integral in (3) requires that the large-scale slope variance $\langle S^2 \rangle$ be specified. In order to relate the emissivity and surface scattering to the friction velocity U_*, we determine a relationship between $\langle S^2 \rangle$ and U_* by calculating the ratio of the h-pol sea-surface reflectivity to the v-pol reflectivity [Wilheit, 1979]. This ratio is given by

$$R^h/R^v = (R_r^h/R_r^v)\ (1 + G^h)/(1 + G^v) \qquad (48)$$

$$G^p = [F/(1 - F)]\ (R_I^p/R_r^p) \qquad (49)$$

where the superscripts denote polarization, with p equaling h or v. The term G^p is proportional to the fractional foam coverage, which is small compared to unity. Hence G^p is small, and (48) can be expanded in terms of G^p. Expanding to first-order gives

$$R^h/R^v = (R_r^h/R_r^v)\ (1 + G^h - G^v) \qquad (50)$$

The above computations of effective foam coverage show that the ratio of foam to water reflectivities is nearly independent of polarization, and the difference between G^h and G^v is typically 0.5%. Thus a very good approximation for the reflectivity ratio is

$$R^h/R^v = R_r^h/R_r^v \qquad (51)$$

The reflectivity ratio on the left-hand side of (51) is found from the SMMR-inferred emissivities discussed above.

$$R^h/R^v = (1 - E_s^h - \Delta E^h)/(1 - E_s^v - \Delta E^v) \qquad (52)$$

The above equation is used to compute a reflectivity ratio for each of the 119 SMMR cells for the two North Pacific SEASAT passes. The SMMR-inferred reflectivity ratios are then regressed versus the collocated SASS-inferred friction velocities U_*. Figure 7 shows the reflectivity ratios plotted versus U_* for 6.6, 10.7, 18, and 37 GHz. The error bars in the figure indicate the uncertainties in the computations due to the error sources discussed above for the SMMR-inferred emissivities. The straight lines in Figure 7 are least squares fits to the data points. These linear regressions have the form

$$R^h/R^v = g_0 + g_1 U_* \qquad (53)$$

The values for g_0 and g_1 are given in Table 6 for

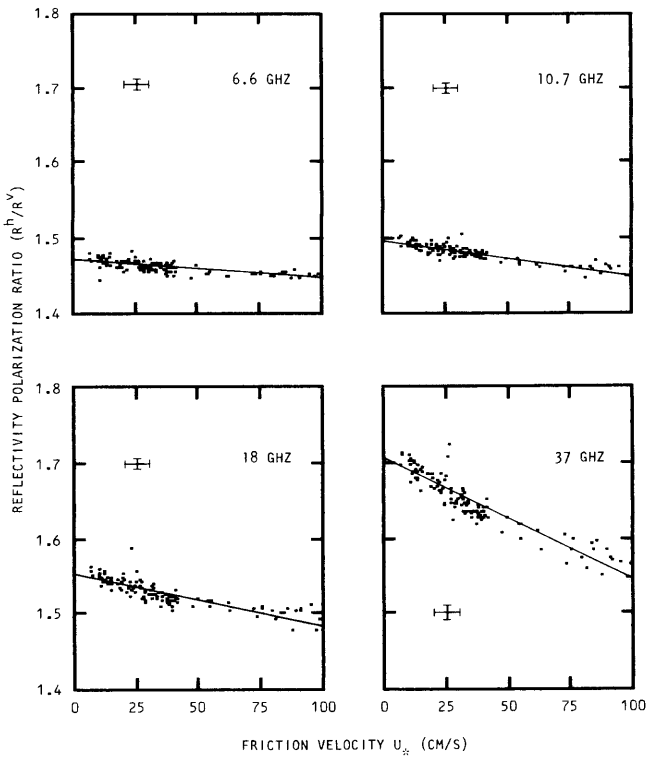

Fig. 7. The ratio of the h-pol sea-surface reflectivity to the v-pol sea-surface reflectivity at four SMMR frequencies.

each SMMR frequency. Because of water vapor contamination, the values for 21 GHz are not directly computed from the SMMR T_B's but rather are interpolations based on the 18 and 37 GHz values. The right-hand side of (51) is calculated from the emissivity integral (4). These computations show that the relationship between the rough-water reflectivity ratio and the large-scale slope variance $\langle S^2 \rangle$ is nearly linear.

$$R_r^h/R_r^v = \bar{g}_0 + \bar{g}_1 \langle S^2 \rangle \qquad (54)$$

The coefficient $\bar{g}_0$ is the reflectivity ratio for a specular sea surface having a zero $\langle S^2 \rangle$. The coefficient $\bar{g}_1$ is found from regressing the emissivity integral computations versus $\langle S^2 \rangle$. The values of the two coefficients appear in Table 6 for each SMMR frequency. Under the assumption that $\langle S^2 \rangle$ equals zero when the friction velocity is zero, the coefficient g_0 in (53) should equal $\bar{g}_0$ in (54). Comparing the two values in Table 6 shows that the two coefficients do agree to within the expected error. Setting g_0 equal to $\bar{g}_0$ and combining (51), (53) and (54) yields the desired relationship between $\langle S^2 \rangle$ and U_*.

$$\langle S^2 \rangle = (g_1/\bar{g}_1)\ U_* \qquad (55)$$

The value of the g ratio is given in Table 6. These values are in good agreement with those reported by Wilheit [1979].

The values of $\langle S^2 \rangle$ given by (55) for the five

TABLE 6. Regression Coefficients for Reflectivity Ratio

Frequency (GHz)	g_0	$\bar{g}_0$	g_1 (s/cm)	$\bar{g}_1$	$g_1/\bar{g}_1$ (s/cm)
6.6	1.471	1.484	-2.5×10^{-4}	-0.701	3.57×10^{-4}
10.7	1.496	1.506	-4.8×10^{-4}	-0.700	6.86×10^{-4}
18	1.551	1.555	-6.7×10^{-4}	-0.837	8.00×10^{-4}
21	1.575	1.577	-8.2×10^{-4}	-0.906	9.05×10^{-4}
37	1.705	1.710	-16.1×10^{-4}	-1.316	12.23×10^{-4}

SMMR frequencies are shown by the solid circles in Figure 8. In this figure the value for U_* is set at 50 cm/s. The solid line in the figure is the slope variance computed from an elevation spectrum of a wind-roughened sea surface [Bjerkass and Riedel, 1979]. The SASS indicates that the capillary portion of this spectrum is a factor of 2 too large. In other words, the capillary waves seen by the SASS in the open ocean are smaller that those observed in the wavetank experiments. Accordingly we divided the capillary portion of the Bjerkass spectrum by a factor of 2 before computing $\langle S^2 \rangle$. The spectrum is partitioned into a large-scale spectrum and a small-scale spectrum according to the criteria that the small-scale height equals the radiation wavelength divided by 8π [Wentz, 1975]. The large-scale spectrum consists of sea waves having wavelengths large compared to the radiation wavelength. An integration over this spectrum yields the large-scale slope variance shown by the solid line. Also shown in the figure is the $\langle S^2 \rangle$ inferred from the SASS nadir NRCS and the $\langle S^2 \rangle$ observed by Cox and Munk [1954]. The Cox and Munk value corresponds to the total slope variance and hence is plotted at 1000 GHz. At this frequency the entire sea spectrum is classified as large-scale. The figure shows very good agreement among the various estimates of $\langle S^2 \rangle$. The largest discrepancy is that the SMMR-inferred slope variance increases faster with frequency than the slope variance obtained from partitioning the wave spectrum.

In summary, the SMMR and SASS observations are combined to obtain the wind-induced emissivity as a function of friction velocity. The emissivity integral (4) is then used to separate the foam emissivity from the rough-water emissivity, thereby obtaining the effective fractional foam coverage. The emissivity integral is also used in conjunction with the SMMR/SASS observations to determine the relationship between the large-scale sea-surface slope variance and the friction velocity. The results are in good agreement with values found by other experimenters. In particular, the foam coverage observed by the SMMR correlates reasonably well with photographic measurements of whitecap coverage. In the case of foam, it appears that whitecaps, rather than streaks, are responsible for the increase in T_B. Also the frequency and polarization variations of the foam reflectivity inferred from the SMMR T_B's are in good agreement with that predicted by a theoretical foam layer model. Finally, the SMMR-inferred large-scale slope variances are consistent with the slope variances computed from a sea elevation spectrum, with that inferred from the SASS nadir observations, and with the Cox and Munk value deduced from sun glitter. The consistency of these results support the premise that the sea-surface emissivity is accurately represented by a composite model in which the emission from the rough

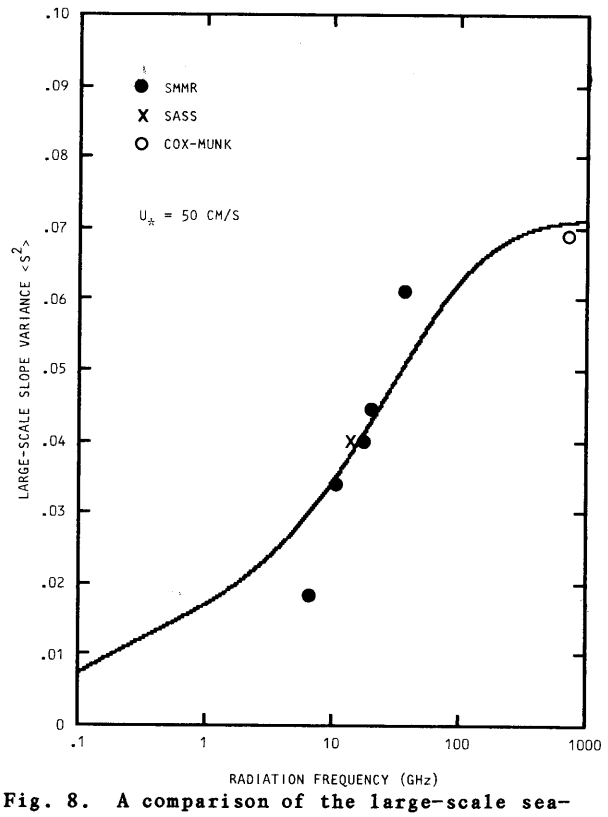

Fig. 8. A comparison of the large-scale sea-surface slope variances obtained from the SMMR data, from a sea wave spectrum, from nadir scatterometer measurements, and from sun glitter observations.

TABLE 7. Model Accuracy Relative to Integral Formulation

SMMR Channel	Model Accuracy (K)
6.6 V	0.2
6.6 H	0.2
10.7 V	0.3
10.7 H	0.3
18 V	0.7
18 H	0.9
21 V	0.9
21 H	1.5
37 V	1.3
37 H	2.1

water is given by two-scale scattering theory and the foam emission is given by a layered dielectric theory.

6. Conclusions

Our basic conclusion is that the T_B model function (27) is an accurate representation of the ocean brightness temperature. The model function is in close agreement to the more precise integral formulation (8). Table 7 lists the rms difference between the model function T_B and the T_B given by (8). These differences are an average over an ensemble of winds and atmospheres ranging from a specular surface and clear skies to a 21 m/s wind and a very heavy cloud layer containing 60 mg/cm² of liquid water. The values in Table 7 are a root-sum-squared of the rms accuracy of the diffuse scattering function I_Ω (14) and the rms accuracy of the atmosphere model given in Table 3. Note that the I_Ω accuracies in Table 1 are with respect to the scattered brightness temperature at the surface, whereas the model function is for the upwelling T_B at the top of the atmosphere. Hence when calculating the values for Table 7, the differences between I_Ω and the scattering integral are first multiplied by the atmospheric transmittance τ before computing the rms statistics.

Another model error is the specification of the sea-surface specular brightness temperature $E_s T_s$ given by (38). Klein and Swift [1977] report an absolute accuracy between 0.1 and 0.3 K in the specular T_B. The major effect of this error is to introduce a constant bias for a given frequency into the model function. Since the error is a bias rather than being random, it is not included in the error statistics in Table 7. For most applications a 0.1 to 0.3 K constant bias in the model function is of no serious consequence.

There is no direct way to determine the error in modeling the wind-induced emissivity ΔE because the sea-surface scattering theory is not precise enough to compare against. The same can be said about the error in modeling rain because of the complexity of the theory for Mie scattering from an array of rain drops. However, an indication of the ΔE error is obtained by looking at the model function's performance in retrieving wind speed via least squares estimation. The retrieval accuracies are about 1.5 m/s, which corresponds to a 10% error in ΔE [Wentz et al., 1982].

In addition, the following conclusions are made concerning the physics of microwaves interacting with the atmosphere and sea surface.

1. When the absorption-emission approximation to the radiative transfer equation is applied to rain clouds, the Mie absorption coefficients rather than the Rayleigh coefficients should be used.

2. The sea-surface emissivity is accurately represented by a composite model in which the emission from the rough water is given by two-scale scattering theory and the foam emission is given by a layered dielectric theory.

3. The large-scale sea-surface slope variance inferred by the SMMR is consistent with the slope variance computed from a sea wave elevation spectrum, with that inferred from microwave scatterometer measurements at nadir, and with the Cox and Munk value deduced from sun glitter.

4. The increase in T_B due to sea foam is more a result of whitecapping than streaking.

5. A layered dielectric model for sea foam predicts the same frequency and polarization variation of the foam reflectivity as observed by the SMMR.

Acknowledgments. This research was sponsored by the SEASAT Data Utilization Project at the Jet Propulsion Laboratory under NASA contract NAS7-100.

References

Barrett, A. H. and V. K. Chung, A Method for the determination of high-altitude water-vapor abundance from ground-based microwave observations, J. Geophys. Res., 67, 4259-4266, 1962.

Bierman, G. J., R. G. Lipes, and F. J. Wentz, Modern estimation techniques applied to microwave sensing of the marine boundary layer, in Proceedings of the 12th Asilomar Conference on Circuits, Systems, and Computers, 101-106, IEEE Computer Society, Pacific Grove, Calif., 1978.

Bjerkaas, A. W., and F. W. Riedel, Proposed model for the elevation spectrum of a wind-roughened sea surface, Tech. Rep. JHU/APL TG 1328, Johns Hopkins Univ., Laurel, Maryland, December 1979.

Brekhovskikh, L. M., Waves in Layered Media, 44-61, Academic, New York, 1960.

Cox, C. S., and W. H. Munk, Measurement of the roughness of the sea surface from photographs of the sun's glitter', J. Opt. Soc. Am., 44, 838-850, 1954.

Deirmendjian, D., Electromagnetic Scattering on Spherical Polydispersions, Elsevier, New York, 1969.

Goldstein, H., Attenuation by condensed water, in Propagation of Short Radio Waves, MIT Radiation Lab. Ser., Vol. 13, McGraw-Hill, New York, 1951.

Grody, N. C., Remote sensing of atmospheric water content from satellites using microwave radiometry, IEEE Trans. Antennas Propagat., AP-24, 155-162, 1976.

Jones, W. L., et al., The SEASAT-A Satellite Scatterometer: The geophysical evaluation of remotely sensed wind vectors over the ocean, J. Geophys. Res., 87, 3297, 1982.

Klein, L. A., and C. T. Swift, An improved model for the dielectric constant of sea water at microwave frequencies, IEEE J. Oceanic Eng., OE-2, 104-111, 1977.

Meeks, M. L. and A. E. Lilley, The microwave spectrum of oxygen in the earth's atmosphere, J. Geophys. Res., 68, 1683-1703, 1963.

Peake, W. H., Interaction of electromagnetic waves with some natural surfaces, IREE Trans. Antennas Propagat., AP-7, S324-S329, 1959.

Ross, D. B., and V. Cardone, Observations of oceanic whitecaps and their relation to remote measurements of surface wind speed, J. Geophys. Res., 79, 444-452, 1974.

Stogryn, A., The apparent temperature of the sea at microwave frequencies, IEEE Trans. Antennas Propagat., AP-15, 278-286, 1967.

Tsang, L., J. A. Kong, E. Njoku, D. H. Staelin, and J. W. Waters, Theory for microwave thermal emission from a layer of cloud or rain, IEEE Trans. Antennas Propagat., AP-25, 650-657, 1977.

Webster, W. J., T. T. Wilheit, D. B. Ross, and P. Gloersen, Spectral characteristics of the microwave emission from a wind-driven foam-covered sea, J. Geophys. Res., 81, 3095-3099, 1976.

Wentz, F. J., The effect of surface roughness on microwave sea brightness temperatures, Contract Rep. 3-35345, Nat. Environ. Satellite Serv., NOAA, Washington, D.C., March 1974.

Wentz, F. J., A two-scale scattering model for foam-free sea microwave brightness temperatures', J. Geophys. Res., 80, 3441-3446, 1975.

Wentz, F. J., A two-scale scattering model with application to the JONSWAP '75 aircraft microwave scatterometer experiment, NASA Contractor Rep. 2919, December 1977.

Wentz, F. J., and H. E. Stumpf, Marine climatic statistics for microwave remote sensing, RSS Tech. Rep. N00173-0288, Remote Sensing Systems, Sausalito, Calif., May 1978.

Wentz, F. J., E. J. Christensen, and K. A. Richardson, Dependence of sea-surface microwave emissivity on friction velocity as derived from SMMR/SASS, in Oceanography from Space, 741-750, Plenum, New York, 1981a.

Wentz, F. J., E. J. Christensen, and K. A. Richardson, Comparison of SEASAT SMMR geophysical algorithms, RSS Tech. Rep., Remote Sensing Systems, Sausalito, Calif., June 1981b.

Wentz, F. J., V. J. Cardone, and L. S. Fedor, Intercomparison of wind speeds inferred by the SASS, altimeter, and SMMR', J. Geophys. Res., 87, 3378, 1982.

Wilheit, T. T., The effect of wind on the microwave emission from the ocean's surface at 37 GHz, J. Geophys. Res., 84, 4921-4926, 1979.

Wilheit, T. T., and A. T. C. Chang, An algorithm for retrieval of ocean surface and atmospheric parameters from the observations of the scanning multichannel microwave radiometer, Radio Sci., 15, 525-544, 1980.

Wu, S. T., and A. K. Fung, A noncoherent model for microwave emissions and backscattering from the sea surface, J. Geophys. Res., 77, 5917-5929, 1972.

(Received August 31, 1981;
revised February 2, 1982;
accepted February 2, 1982)